Dual-bioinspired MetaGels integrating heat buffering and radiative cooling for ultrahigh-power thermal management

Gangchen Lu [1], Shiliang Zhang [2], Xianrong Huang [1], Yang Ding [1], Xiangyu Zhao [1], Bingqing Quan [1], Xinpeng Hu [1], Guangming Tao [2, 3] *, Jinping Qu [1, 4], Xiang Lu [1] *

[1] *Key Laboratory of Material Chemistry for Energy Conversion and Storage, Ministry of Education; Hubei Key Laboratory of Material Chemistry and Service Failure; Hubei Key Laboratory of Bioinorganic Chemistry and Materia Medica and Hubei Engineering Research Center for Biomaterials and Medical Protective Materials; School of Chemistry and Chemical Engineering, Huazhong University of Science and Technology, Wuhan, Hubei, 430074, China.*

[2] *Research Center for Intelligent Fiber Devices and Equipment, Wuhan National Laboratory for Optoelectronics, School of Materials Science and Engineering, School of Physical Education, Huazhong University of Science and Technology, Wuhan 430074, China.*

[3] *Center for Intelligent Health Interdisciplinary Science, Central China Normal University, Wuhan 430079, China.*

[4] *National Engineering Research Center of Novel Equipment for Polymer Processing; Key Laboratory of Polymer Processing Engineering, Ministry of Education, School of Mechanical and Automotive Engineering, South China University of Technology, 510641, Guangzhou, China.*

These authors contributed equally: Gangchen Lu, Shiliang Zhang

Corresponding authors: Guangming Tao (tao@hust.edu.cn), Xiang Lu (luxiang@hust.edu.cn & luxiang_1028@163.com)

Solar reflectance and MIR emittance calculations[1]

The equation for calculating the average solar reflectance (R_{solar}, 0.3-2.5 μm) of the sample is

$$R_{solar} = \frac{\int_{0.3}^{2.5} I_{solar}(\lambda) R(\lambda)\, d\lambda}{\int_{0.3}^{2.5} I_{solar}(\lambda)\, d\lambda} \quad (1)$$

where $I_{solar}(\lambda)$ is the ASTM G173-03 AM1.5 Global Tilt spectrum. $R(\lambda)$ is the measured spectral reflectance of the sample.

The equation for calculating the mean emittance in the atmospheric window (ε, 8-13 μm) of the sample is

$$\varepsilon = \frac{\int_{8}^{13} I_{bb}(T,\lambda)\varepsilon(\lambda)\, d\lambda}{\int_{8}^{13} I_{bb}(T,\lambda)\, d\lambda} \quad (2)$$

where $I_{bb}(T,\lambda)$ and $\varepsilon(\lambda)$ are the blackbody radiation intensity and the measured spectral emittance of the sample, respectively (λ is wavelength).

The $I_{bb}(T,\lambda)$ can be calculated from

$$I_{bb}(T,\lambda) = \frac{4\pi c^2 h}{\lambda^5} \frac{1}{e^{\frac{2\pi hc}{\lambda k_B T}} - 1} \quad (3)$$

where c, h, and k_B are the speed of light (3×10^8 m s^{-1}), the reduced Planck constant (1.055×10^{-34} J s), and Boltzmann constant (1.381×10^{-23} J K^{-1}), respectively.

Thermal transfer simulations

The thermal transfer simulations were performed using COMSOL Multiphysics software. We simulated the emulgel structure using a three-dimensional (3D) model. The heat conduction simulations were confined to a 40 cm × 40 cm × 40 cm cubic region within the emulgels. Spheres dispersed in emulgels were randomly generated

and represented PCM. Based on prior measurements of the emulgels, the thermal conductivity of the polymer framework within B0P20 was set to 1 W m^{-1} K^{-1}, while that within B8P20 was set to 10 W m^{-1} K^{-1}. The PCM was uniformly assigned a thermal conductivity of 0.2 W m^{-1} K^{-1} and a latent heat of 216 J g^{-1}. A constant temperature of 353 K (80 °C) was applied to the bottom surface, while all other surfaces were configured as thermally insulated. Fig. 3f corresponds to the cross-sectional result of the simulation at y = 0.

Interpretation of the capillary forces in MetaGel during the drying process.

During the drying process of MetaGel, the evaporation of the solvent creates a liquid-vapor interface within the nanopores of the polymer network. The resulting capillary pressure (ΔP) can be described by the Young-Laplace equation.

$$\Delta P = \frac{2\gamma cos\theta}{r} \quad (4)$$

where γ is the surface tension of water, θ is the contact angle, and r is the radius of the pore. This capillary pressure exerts a large inward compressive stress on the gel skeleton. As the gel network is physically compressed, the distance between polymer chains is drastically reduced. This forced proximity overcomes steric hindrance, allowing for the reestablishment of inter-chain and interfacial hydrogen bonds.[2]

The capillary forces change significantly over time during the drying process. As drying progresses, the water content decreases, causing the gel network to shrink and the average r to continuously decrease. According to the Young-Laplace equation, ΔP

increases inversely with the decreasing pore size. Thus, the compressive force strengthens over time, accelerating densification and hydrogen bond formation. The capillary force reaches its maximum before the complete depletion of the water. Once the water has fully evaporated, the liquid-vapor interface disappears, and the dynamic capillary forces cease, leaving behind a structurally locked and highly hydrogen-bonded network.

Temperature affects the evaporation rate of water. At higher temperatures, rapid evaporation causes a sharp increase in capillary forces over a very short time. This fast drying can lead to severe stress gradients across the MetaGel, potentially causing non-uniform structural transformation or even micro-cracking at the surface. Conversely, drying at a lower, controlled temperature allows for a slower, more uniform buildup of capillary forces, which gives the polymer chains sufficient time to rearrange and re-establish strong hydrogen bonds without structural defects.

The factors influencing the oven-drying process include not only temperature and drying time but also wind speed. Gong’s group discovered that as the drying time increases, the hydrogel's microstructure is continuously oriented and its internal hydrogen bonds are altered. This process has an impact on the material's strength and toughness.[3] Majidi’s group found that different drying times had a large effect on the conductivity of conductive hydrogels.[4] As a result, we believe that adjusting the drying airflow rate or applying a temperature gradient over time could yield interesting results.

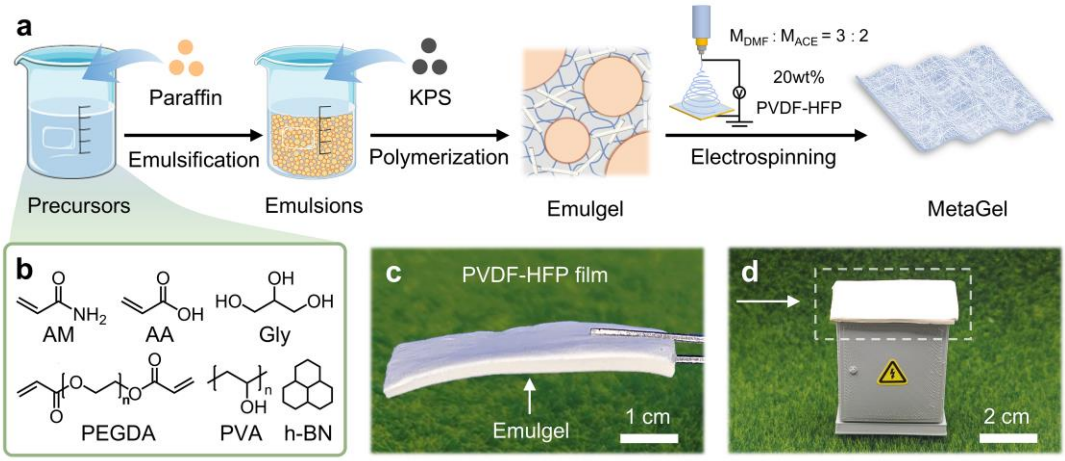

Figure S1. a) Synthesis pathway illustration of the MetaGel. b) Chemical components of the emulgel polymer network. c) Combination of the emulgel and PVDF-HFP film in the MetaGel. d) The photograph of the MetaGel attached to the power distribution box model.

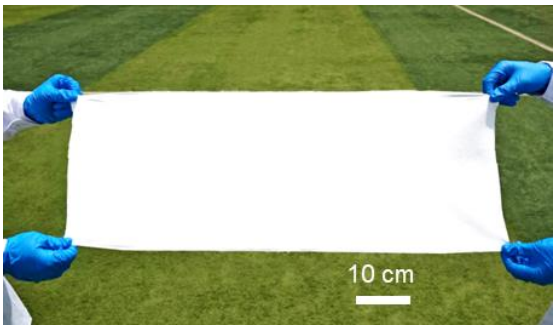

Figure S2. Optical photograph of the PVDF-HFP film.

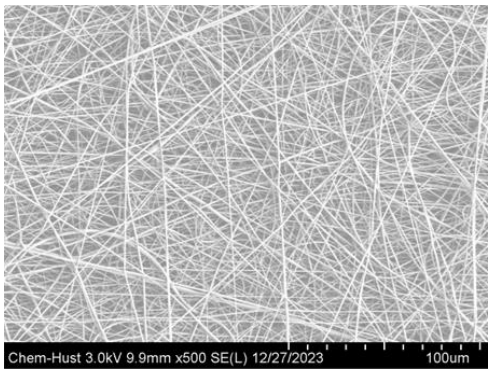

Figure S3. The SEM image of PVDF-HFP film.

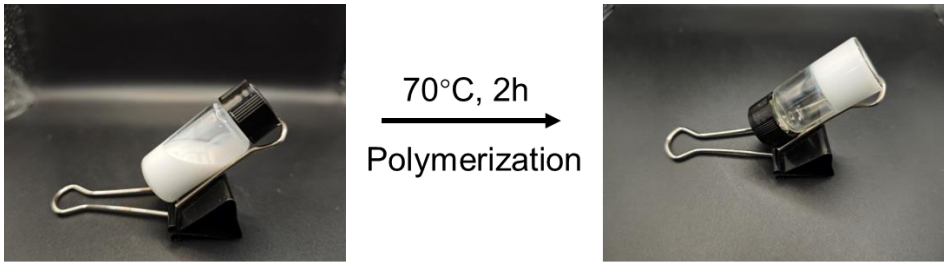

Figure S4. Preparation of the phase change emulgel via thermally initiated polymerization at 70 °C for 2 h. Photos of the oil-in-water emulsion before polymerization (left) and the resulting emulgel (right).

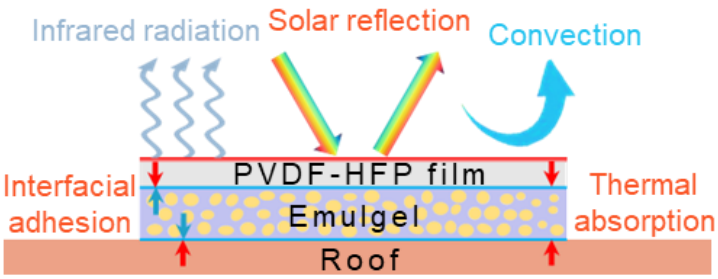

Figure S5. The role and combination of components in the MetaGel.

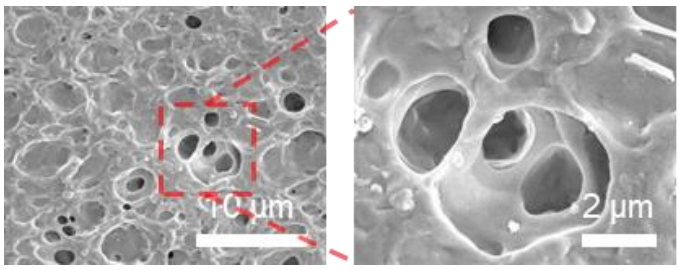

Figure S6. Cross-sectional SEM image of the emulgel and the expanded version.

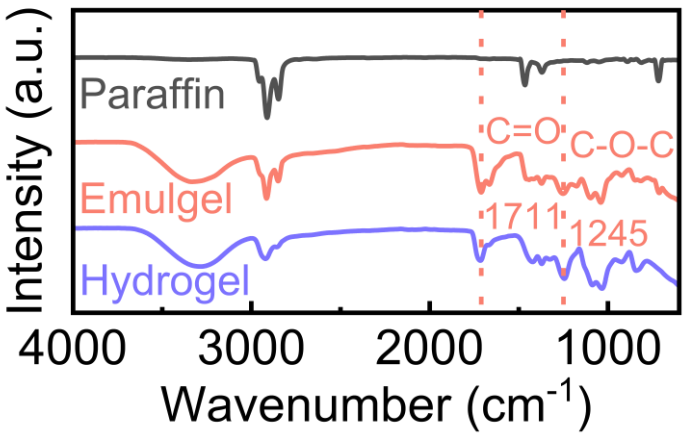

Figure S7. FTIR spectrum of paraffin, the emulgel, and the hydrogel.

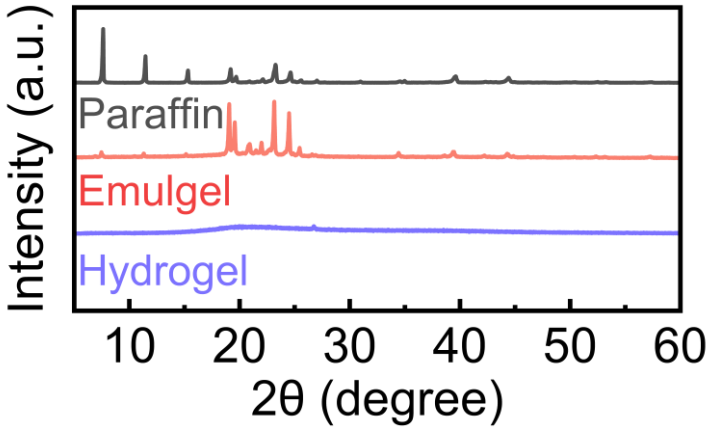

Figure S8. XRD patterns of paraffin, the emulgel, and the hydrogel.

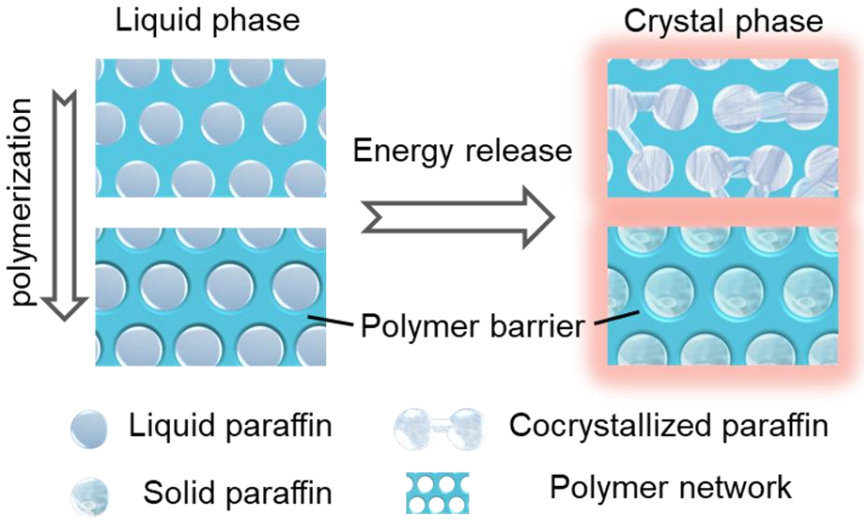

Figure S9. Flexible mechanism of the emulgel at room temperature.

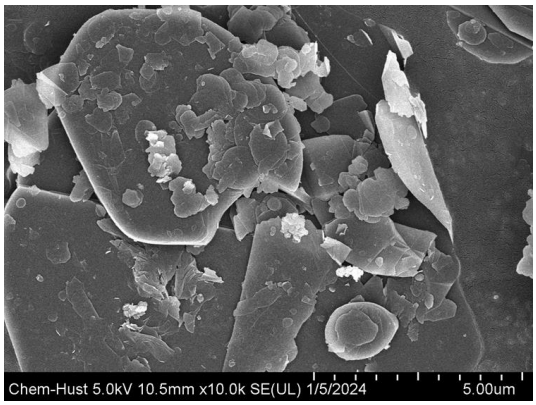

Figure S10. The FESEM image of the h-BN sheets. The diameter of h-BN is within 5 and 10 μm.

Table S1. BXP20 Recipes

	B0P20	B2P20	B4P20	B6P20	B8P20	B10P20
Continuous Phase (g)						
PVA (8wt %)	15.00	15.00	15.00	15.00	15.00	15.00
h-BN	0.00	2.00	4.00	6.00	8.00	10.00
AM	1.00	1.00	1.00	1.00	1.00	1.00
AA	3.00	3.00	3.00	3.00	3.00	3.00
PEGDA	0.20	0.20	0.20	0.20	0.2	0.2
Glycerol	3.00	3.00	3.00	3.00	3.00	3.00
H_2O	17.70	15.70	13.70	11.70	9.70	7.70
KPS	0.10	0.10	0.10	0.10	0.10	0.10
Total	40.00	40.00	40.00	40.00	40.00	40.00
Dispersion Phase (g)						
Paraffin	20.00	20.00	20.00	20.00	20.00	20.00

Table S2. DSC heating and cooling characteristics of BXP20s and paraffin

Sample	T_m (℃)	ΔH_m (J/g)	T_c (℃)	ΔH_c (J/g)	η (%)	η* (%)
Paraffin	29.90 ±0.90	216.56 ±0.62	23.47 ±0.46	215.12 ±1.14	100.00	100.00
B0P20	31.16 ±1.50	146.66 ±2.71	16.70 ±0.79	146.22 ±2.34	67.72	70.18
B2P20	30.54 ±0.83	131.04 ±1.89	18.11 ±0.55	131.39 ±1.42	60.51	65.57
B4P20	30.33 ±0.43	125.23 ±4.40	19.29 ±0.64	126.63 ±4.35	57.83	61.54
B6P20	29.94 ±0.32	117.06 ±1.73	19.66 ±0.25	116.98 ±1.22	54.05	57.97
B8P20	29.74 ±0.50	111.86 ±2.50	22.14 ±0.57	112.04 ±2.64	51.65	54.79
B10P20	29.80 ±0.30	105.96 ±2.69	22.22 ±0.17	107.41 ±3.45	48.93	51.95

η is calculated according to the ΔH_m of paraffin and BXP20s and η* is calculated according to the paraffin loading of BXP20s in the formula (Table S1).

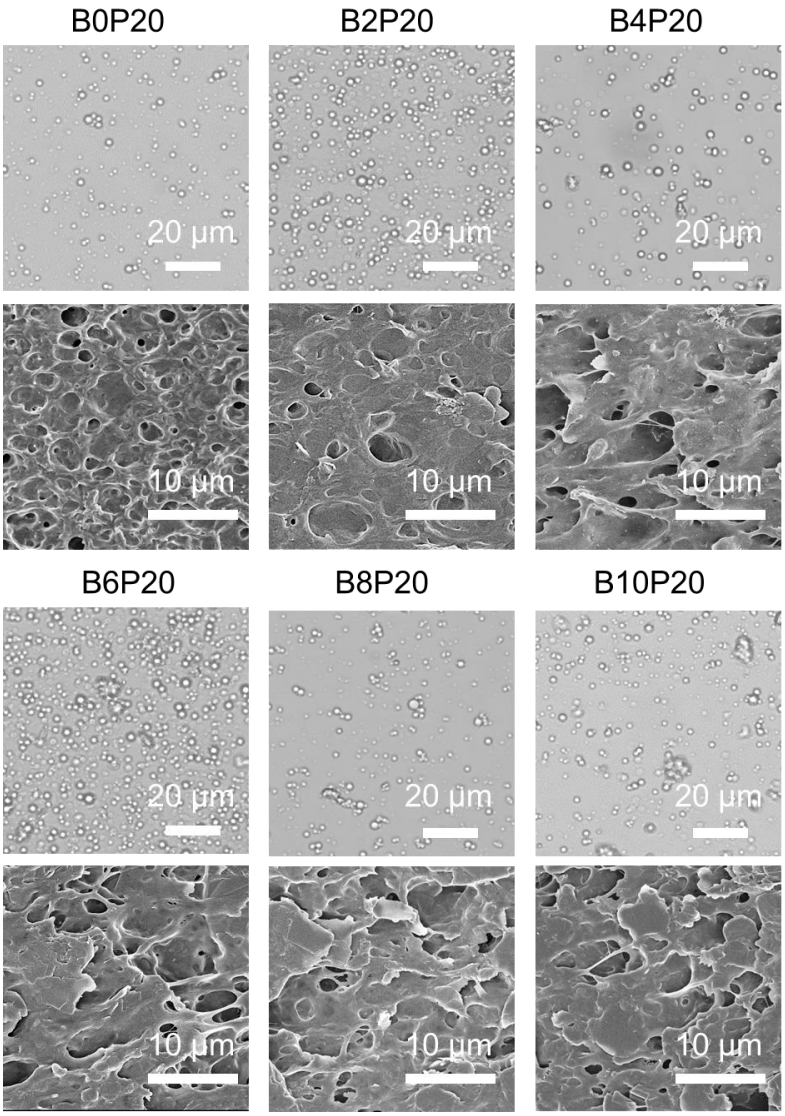

Figure S11. Optical microscope images of the emulsions and FESEM images of the emulgels with different h-BN loadings. As the content of h-BN increases, the layered heat conduction pathways become more pronounced.

Figure S12. Images of an emulgel loading with 500g at 10°C.

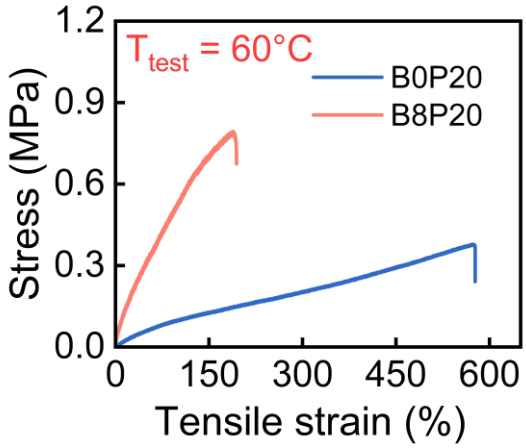

140

141 **Figure S13.** Tensile stress-strain curves of B0P20 and B8P20 at 60 °C.

142

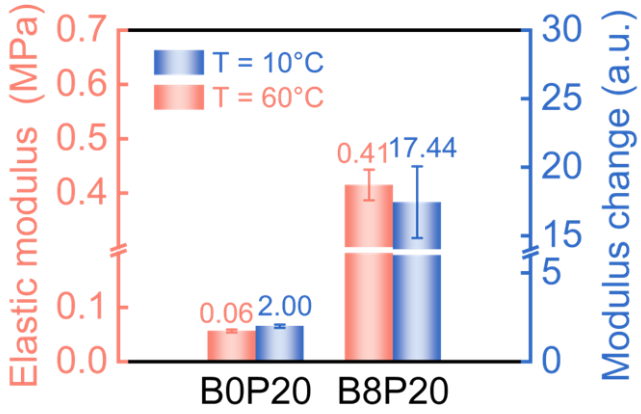

143

144 **Figure S14.** The comparison of elastic modulus of B0P20 and B8P20 at different

145 testing temperatures.

146

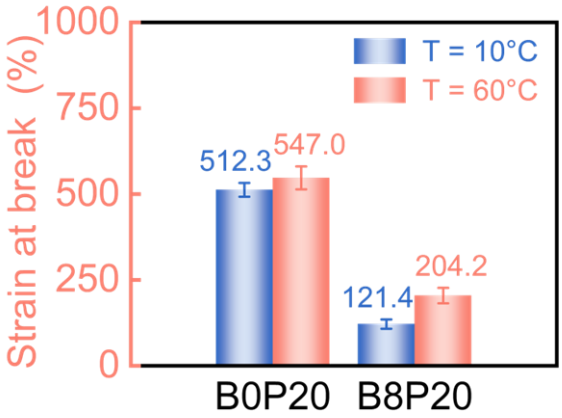

147

148

149 **Figure S15.** Comparison of the fracture strains of B0P20 and B8P20 at different testing

150 temperatures.

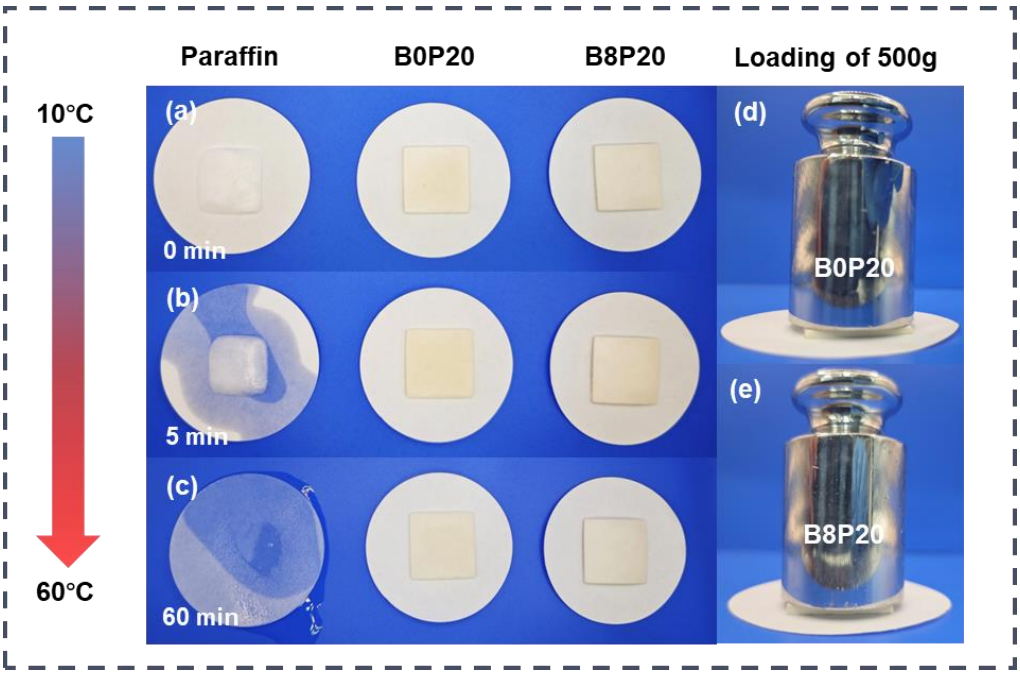

Figure S16. The images show the shape stability of B0P20 and B8P20. The leakage trace of the paraffin is on the respective filter papers after being heated at 60 °C for 60 min. A 500g weight was applied to the each composite after 30 min.

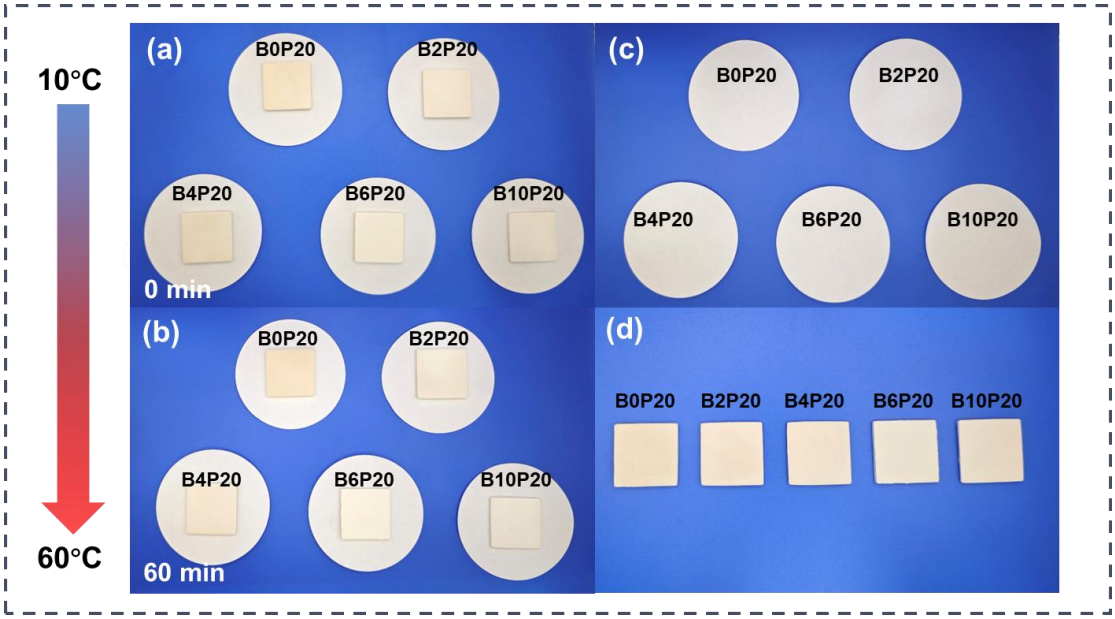

Figure S17. The images show the shape stability of B0P20, B2P20, B4P20, B6P20, and B10P20. The leakage trace of the paraffin is on the respective filter papers after being heated at 60 °C for 60 min.

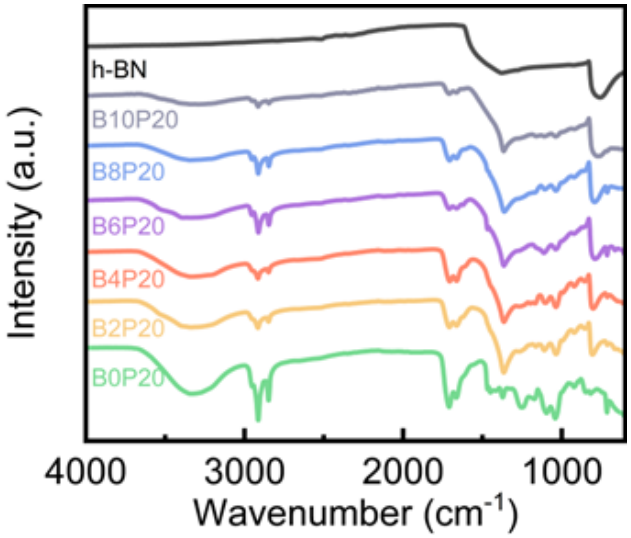

Figure S18. FTIR spectra of h-BN and the emulgels with different h-BN contents.

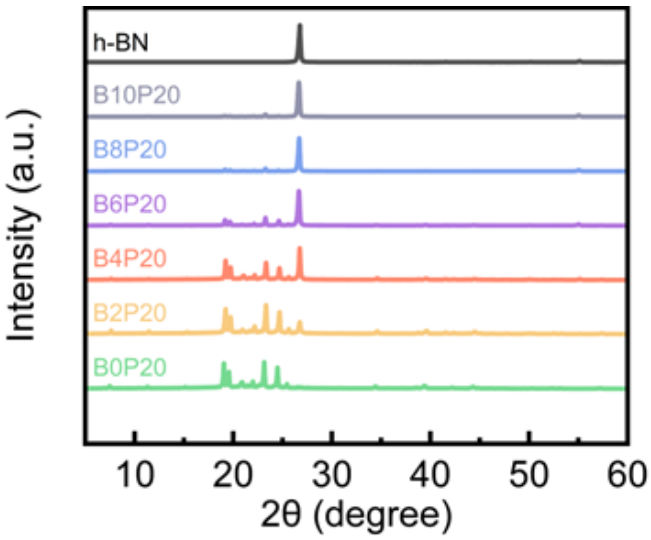

Figure S19. XRD spectra of h-BN and the emulgels with different h-BN contents.

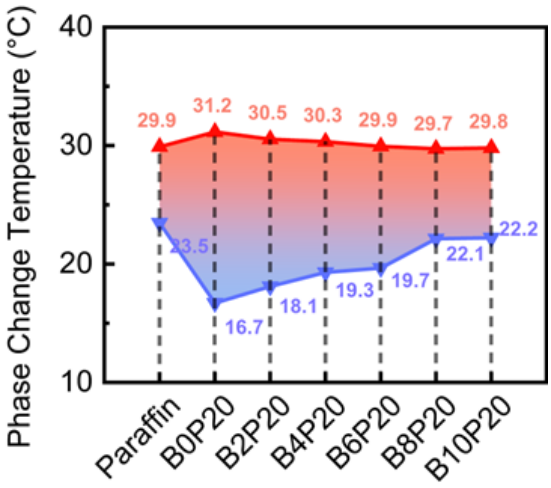

Figure S20. The phase change temperature of paraffin and the emulgels with varying h-BN concentrations.

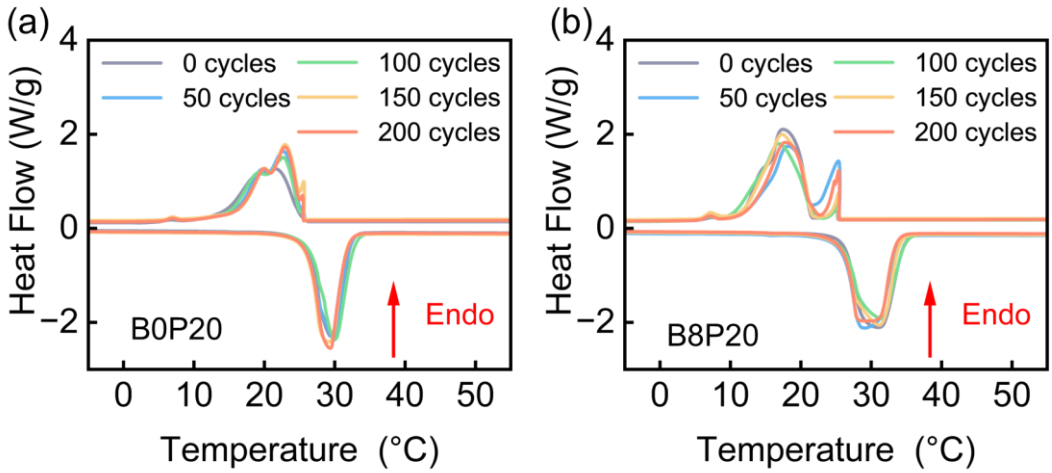

Figure S21. DSC cycle curves of (a) B0P20 and (b) B8P20.

Table S3. DSC heating and cooling characteristics of B0P20 and B8P20 after cycles.

Sample	Cycles	T_m (°C)	ΔH_m (J/g)	T_c (°C)	ΔH_c (J/g)
B0P20	0	31.16	146.66	16.70	146.22
	50	29.04	141.80	18.22	141.70
	100	31.49	139.50	16.92	138.22
	150	31.14	141.36	17.35	140.74
	200	30.09	137.56	17.82	137.45
B8P20	0	29.74	111.86	22.14	112.04
	50	29.91	114.53	22.65	115.11
	100	30.11	113.61	22.72	113.32
	150	29.14	116.19	22.93	116.26
	200	29.36	115.36	22.94	114.92

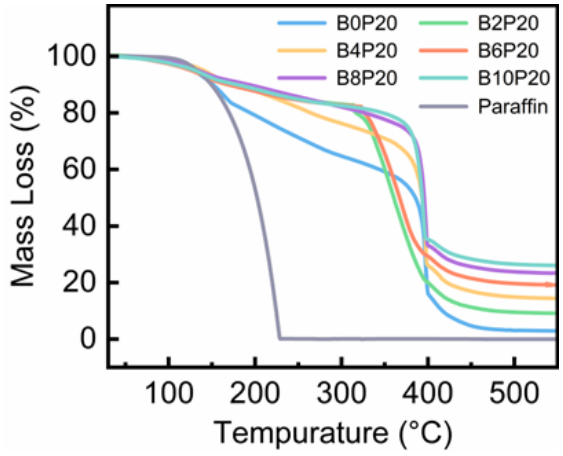

Figure S22. TGA curves of paraffin and the emulgels with varying concentrations of h-BN under a N_2 atmosphere. The residual mass corresponds to the concentrations of h-BN.

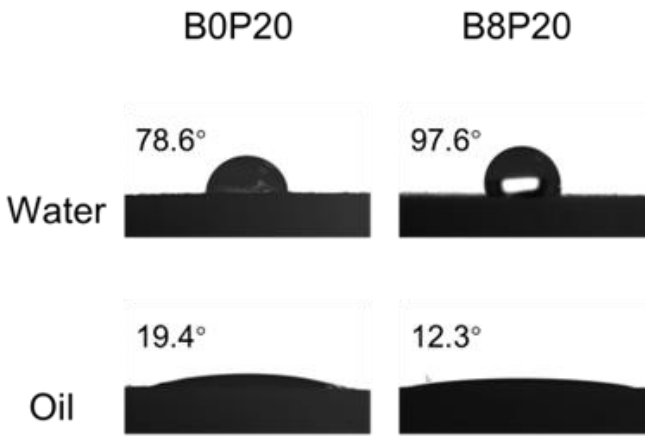

Figure S23. Contact angle measurements of B0P20 and B8P20 using water and oil.

Figure S24. Photographs obtained during the tensile test. The samples were separated at the midpoint.

Table S4. Thermal conductivity and thermal conductivity enhancement characteristics of the BXP20s.

Sample	h-BN content in the dried sample (%)	Thermal conductivity (W m^{-1} K^{-1})	Thermal conductivity enhancement (%)
B0P20	0.00	0.30±0.01	/
B2P20	6.56	0.54±0.01	82.69
B4P20	12.31	0.74±0.01	149.01
B6P20	17.39	0.86±0.03	190.83
B8P20	21.92	1.00±0.01	238.16
B10P20	25.97	1.15±0.02	289.62

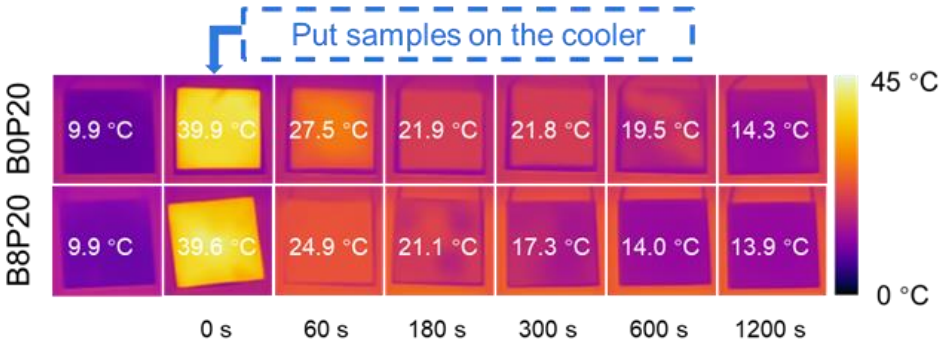

Figure S25. Forward-looking infrared camera images of B0P20 and B8P20 placed on a cold stage at 10 ℃ for 20 min. The samples were equilibrated to 40 ℃ before testing.

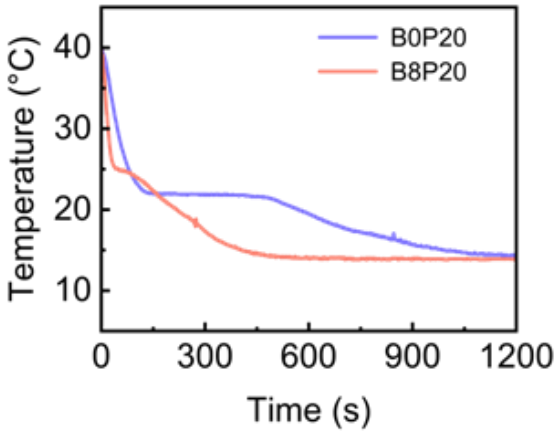

Figure S26. Curves of temperature decrease of B0P20 and B8P20 placed on a cold stage at 10 ℃ for 20 min.

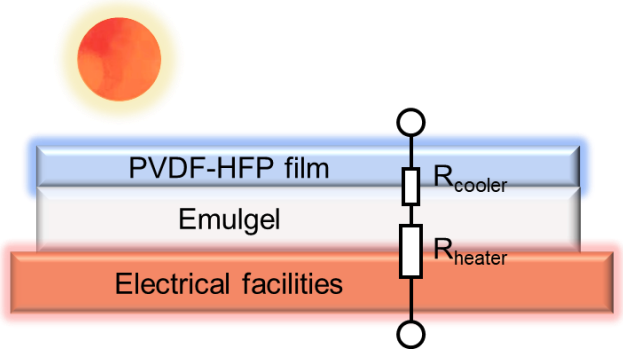

Figure S27. Schematic diagram of the interfacial thermal resistances in the MetaGel during thermal management.

Figure S28. The photographs of the B8P20 attached to various building models.

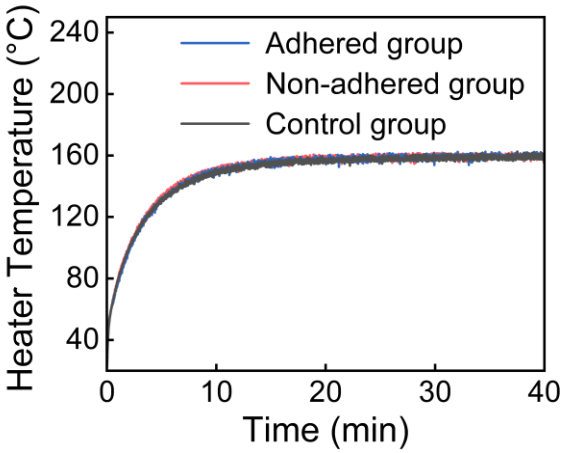

Figure S29. The internal heater temperature variation curves of different groups. The overlapping curves confirmed comparable heating conditions among the different groups.

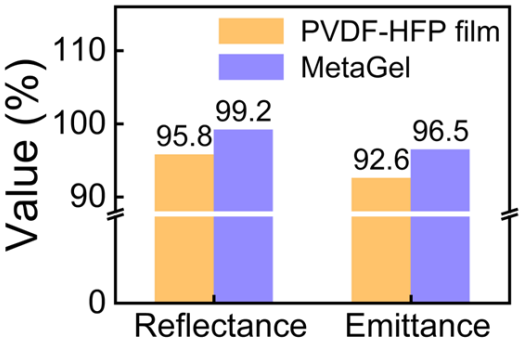

Figure S30. Comparison of the mean solar reflectance and average atmospheric-window emittance of the PVDF-HFP film and the MetaGel.

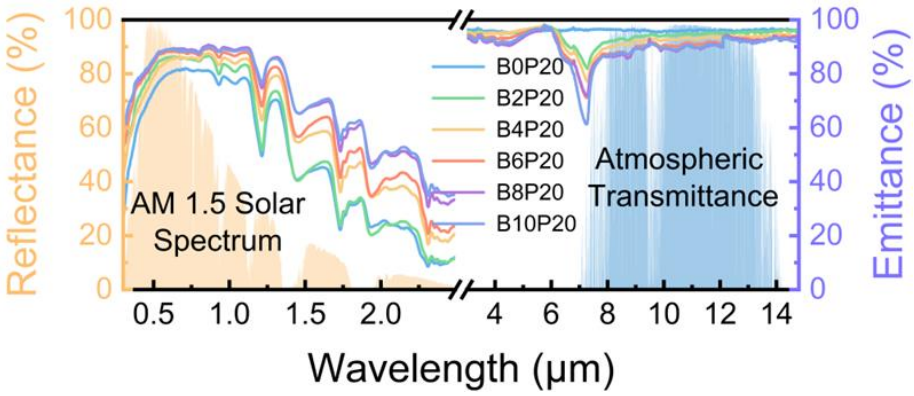

Figure S31. Reflectance spectra at AM1.5 solar spectrum (0.3-2.5 μm) and emissivity spectra at atmospheric window (8-13 μm) of the emulgels with varying h-BN contents.

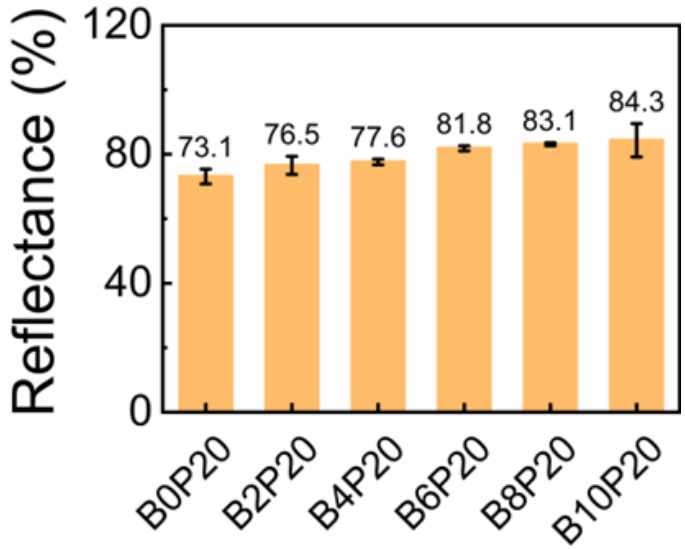

Figure S32. The mean reflectance at AM1.5 solar spectrum (0.3-2.5 μm) of the emulgels with varying h-BN contents.

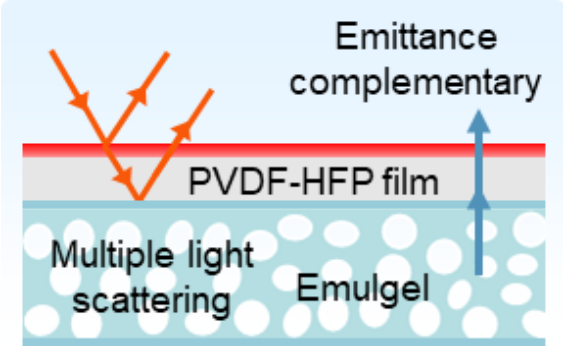

Figure S33. Enhancement mechanisms of reflectance and emittance of the MetaGel compared with the PVDF-HFP film.

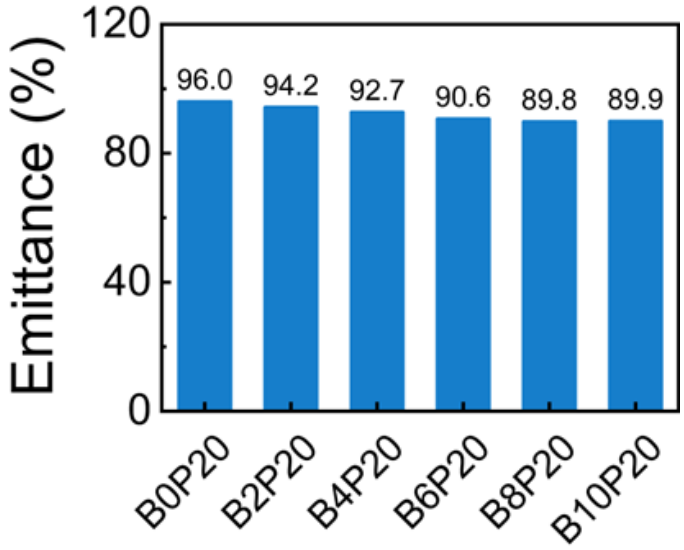

Figure S34. The average emittance at atmospheric window (8-13 μm) of the emulgels with varying h-BN contents.

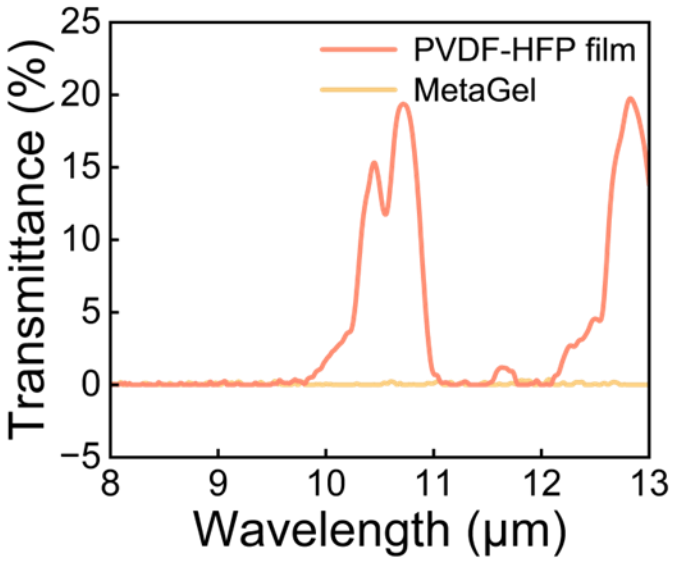

Figure S35. The transmittance of the PVDF-HFP film and MetaGel at atmospheric window (8-13 μm).

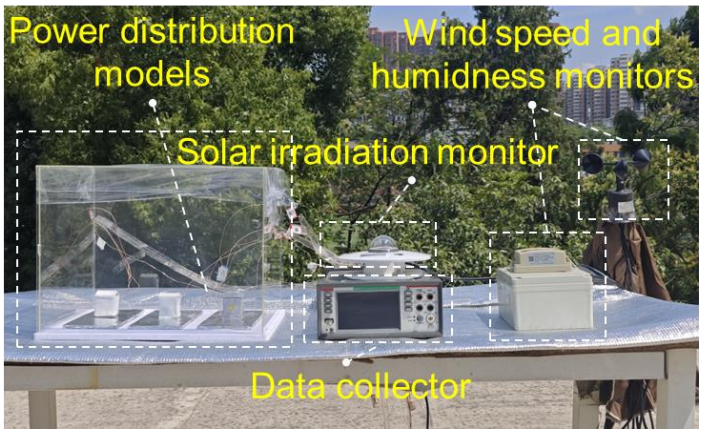

Figure S36. Optical photograph of the device for cooling performance test on May 29, 2025, Wuhan, China.

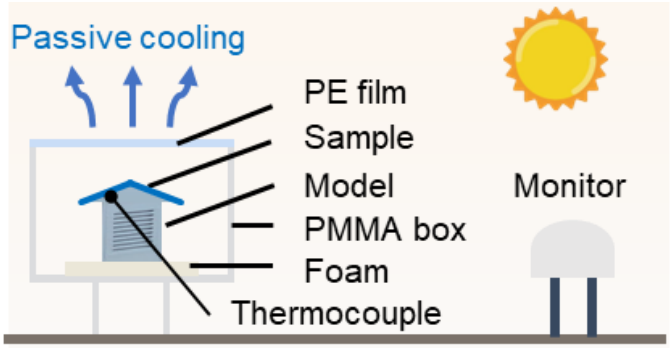

Figure S37. The schematic illustration of the specific test device for cooling performance test on May 29, 2025, Wuhan, China.

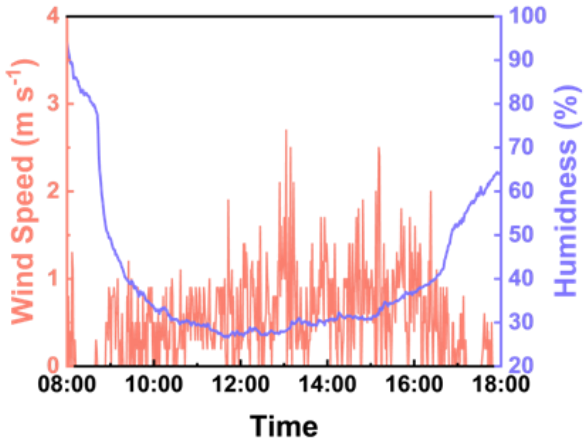

Figure S38. The wind speed and humidness in Wuhan, China from 08:00 to 18:00 on May 29, 2025.

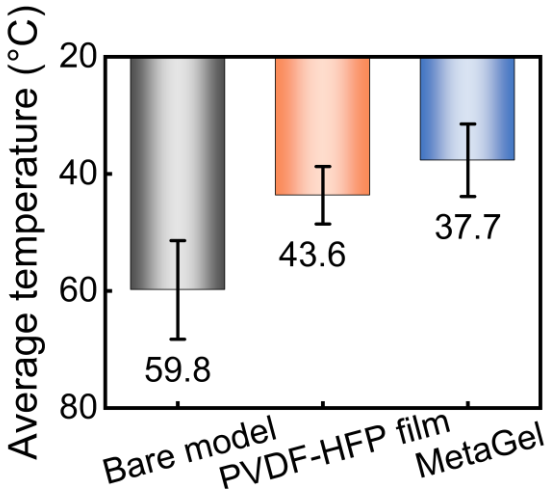

Figure S39. The average temperature charts of the bare model, the PVDF-HFP film and the MetaGel in Wuhan, China, from 08:00 to 18:00 on May 29, 2025.

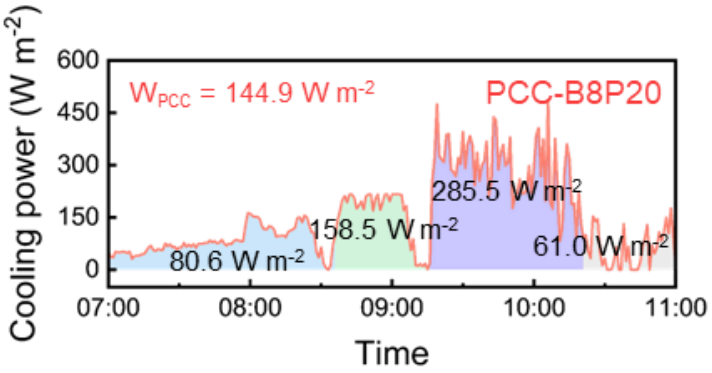

Figure S40. The cooling power curves of the B8P20 sample from 7:00 to 11:00 AM (Sipsongpanna, China on March 25, 2024).

To elucidate the cooling contribution of the phase change layer, we conducted an outdoor cooling power assessment of the B8P20 sample. The testing apparatus was based on a method established in a previous study, in which electrical energy supplied to a polyimide heater was converted into Joule heat to maintain the sample at the ambient temperature. The cooling power of phase change composite (PCC) was illustrated in Fig. S40, revealing an average power of 144.9 W m^{-2} over 4 h. The solar irradiation intensity, wind speed and relative humidity were recorded in Figs. S41 and S42. The results were categorized into four distinct phases. Phase 1, occurring from 7:00 to 8:35 AM, was characterized by ambient temperatures remaining below 20 °C during which the PCM remained inactive, yielding an average power of 80.6 W m^{-2}. Phase 2, spanning from 8:35 to 9:15 AM, approached the initial melting temperature of the paraffin, prompting the surface material to commence melting and resulting in a temperature platform. During this phase, the power output increased to 158.5 W m^{-2}. Phase 3, from 9:15 to 10:20 AM, witnessed a gradual rise in surface temperature,

accompanied by the rapid melting of the PCM, leading to a significant increase in cooling power to 285.5 W m^{-2}. Subsequently, in Phase 4, from 10:20 to 11:00 AM, the phase change process reached completion, with the radiative cooling power of the phase change layer diminishing to 61.0 W m^{-2}. Given that the solar reflectance of B8P20 was approximately 83%, the empirical data aligned with our initial hypotheses, underscoring the pronounced contribution of the PCM to the overall cooling performance.

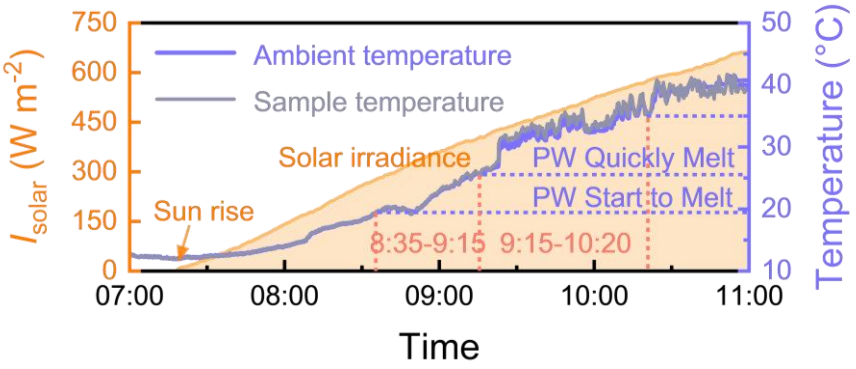

Figure S41. The curves of ambient and sample temperatures and irradiation intensity during the cooling power test of B8P20 in Sipsongpanna, China from 07:00 to 11:00 AM on March 25, 2024.

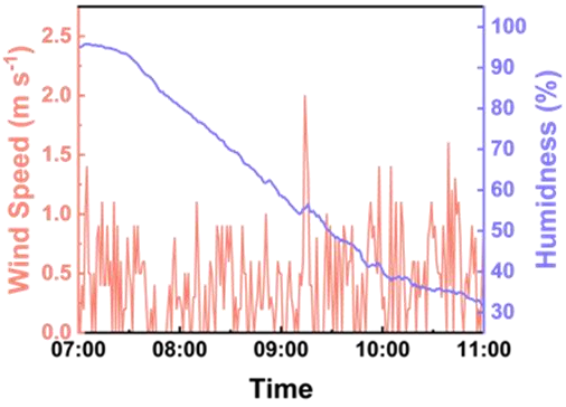

Figure S42. The wind speed and humidness in Sipsongpanna, China from 07:00 to 11:00 AM on March 25, 2024.

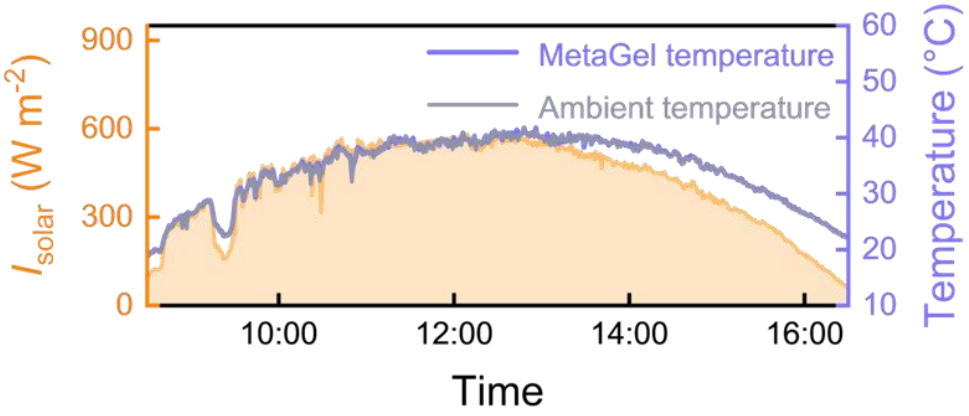

Figure S43. The curves of ambient and sample temperatures and irradiation intensity during the cooling power test of MetaGel in Wuhan, China from 08:30 to 16:30 on November 1, 2024.

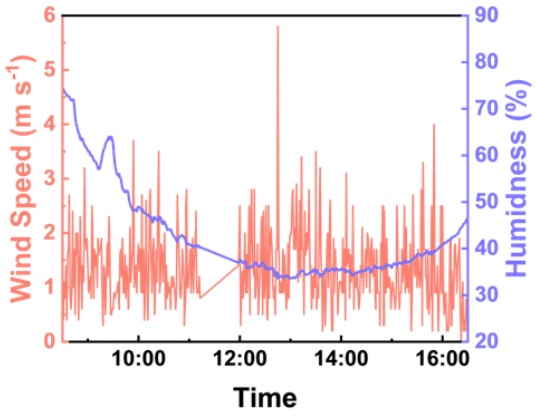

Figure S44. The wind speed and humidness in Wuhan, China from 08:30 to 16:30 on November 1, 2024.

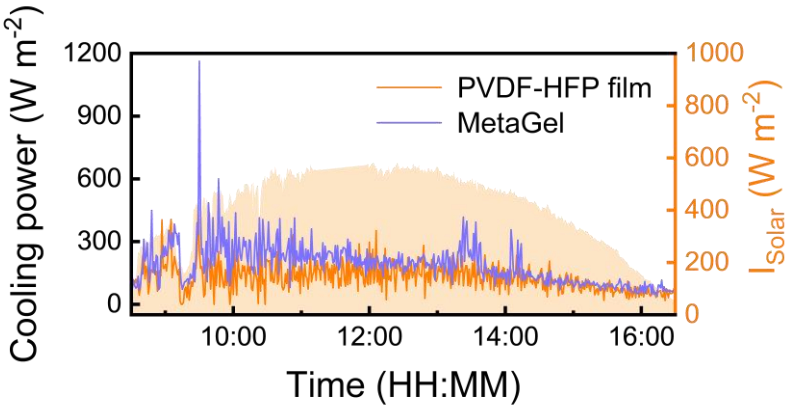

Figure S45. The cooling power curves of the PVDF-HFP film and the MetaGel throughout the day (from 8:30 to 16:30 on November 1, 2024 in Wuhan, China). The integration interval for cooling power calculations was 1 minute.

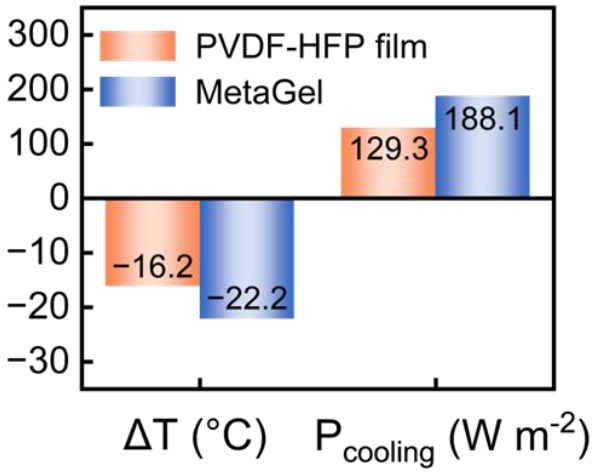

335
336

337 **Figure S46.** The comparison chart of average cooling performance and mean cooling

338 powers between the PVDF-HFP film and the MetaGel.

339

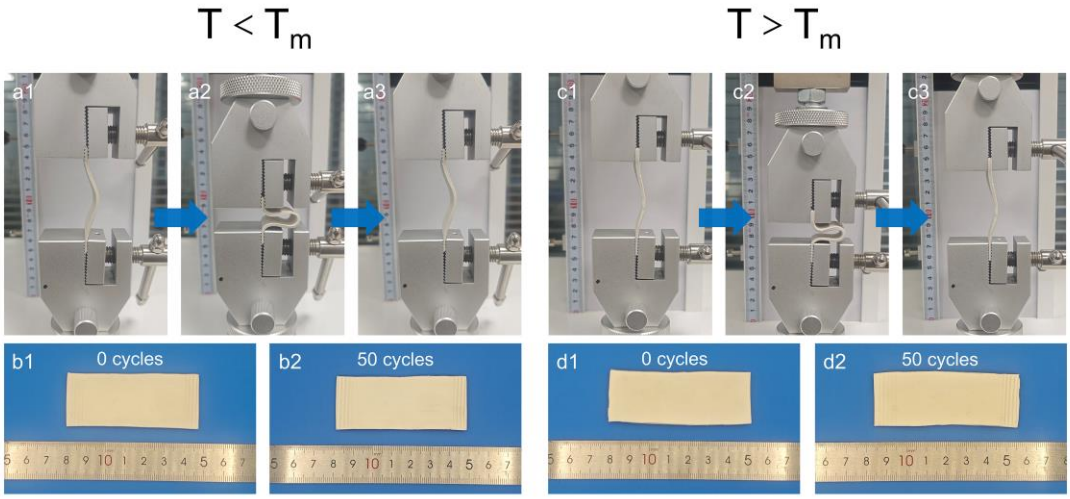

340

341 **Figure S47.** The cyclic bending and stretching performance of the emulgel at different

342 temperatures.

343

344 At temperatures below the melting point of the PCM ($T < T_m$), the sample exhibited a

345 slight elongation after 50 cycles (Figs. S47 b1 and b2). This phenomenon could be

346 attributed to the fact that a portion of the mechanical stress was stored within the

347 composite network and could not be completely dissipated. When the sample was

subsequently heated above the melting temperature ($T > T_m$), the phase transition was triggered, allowing the trapped internal stress to be released (Fig. 2l). Conversely, when the cyclic tests were conducted at temperatures exceeding the melting point ($T > T_m$), the internal PCM was in a liquid state, providing high flexibility and mobility to the emulgel. We found that after 50 cycles, the shape of the emulgel remains virtually unchanged, with almost no residual strain or structural degradation observed. Overall, these cyclic tests indicate that MetaGel possesses robust durability and shape stability across both temperature regimes. Concerning the precise ultimate fatigue limit, we hypothesize that the material can endure several thousand cycles due to its highly flexible polymer network.

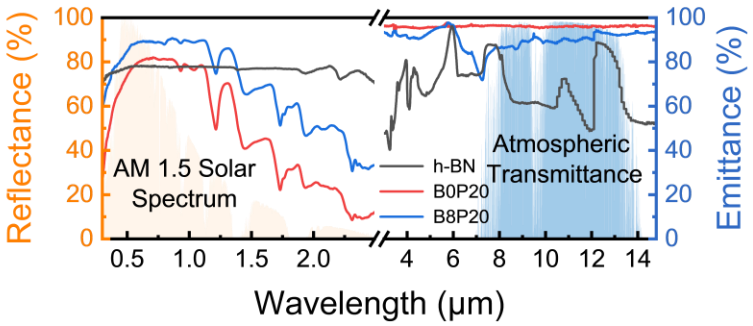

Figure S48. Reflectance spectra at AM1.5 solar spectrum (0.3-2.5 μm) and emissivity spectra at atmospheric window (8-13 μm) of h-BN, B0P20, and B8P20.

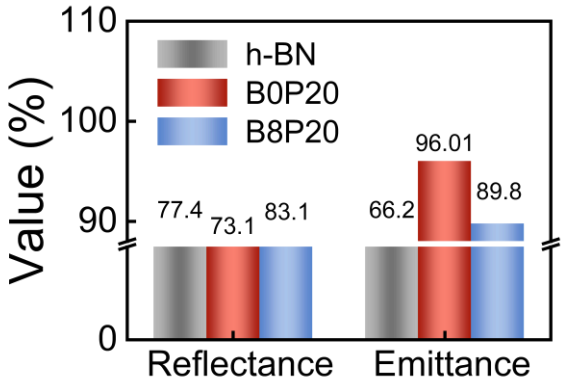

Figure S49. The mean reflectance at AM1.5 solar spectrum (0.3-2.5 μm) and average emittance at atmospheric window (8-13 μm) of h-BN, B0P20, and B8P20.

References:

[1] X. Wu, J. Li, F. Xie, X. E. Wu, S. Zhao, Q. Jiang, S. Zhang, B. Wang, Y. Li, D. Gao, R. Li, F. Wang, Y. Huang, Y. Zhao, Y. Zhang, W. Li, J. Zhu, R. Zhang, Nat. Commun. **2024**, 15, 815.

[2] G. Lu, Y. Zhang, L. Chen, Y. Song, Z. Mao, B. Wang, L. Rong, X. Sui, X. Feng, Chem. Eng. J. **2024**, 493, 152425.

[3] M. T. I. Mredha, Y. Guo, T. Nonoyama, T. Nakajima, T. Kurokawa, J. Gong, Adv. Mater. **2018**, 30, 1704937.

[4] Y. Ohm, C. Pan, M. Ford, X. Huang, J. Liao, C. Majidi, Nat. Electron. **2021**, 4, 185.